water

MDPI

Article

Ozone Catalysis Degradation of Sodium Acetate via Vacancy-Driven Radical Oxidation over Fe-Modified Fly Ash

Yaoji Chen [1], Ruifu Chen [2], Xinglan Chang [1], Jingying Yan [1], Yajie Gu [1], Shuang Xi [1], Pengfei Sun [2,*] and Xiaoping Dong [2]

[1] Zhejiang Tiandi Environmental Protection Technology Co., Ltd., 2159-1 Yuhangtang Road, Hangzhou 311199, China; elo1989@163.com (X.C.)
[2] Key Laboratory of Surface & Interface Science of Polymer Materials of Zhejiang Province, School of Chemistry and Chemical Engineering, Zhejiang Sci-Tech University, 928 Second Avenue, Xiasha Higher Education Zone, Hangzhou 310018, China
* Correspondence: sunpf@zju.edu.cn

Abstract: In order to realize the high value-added reuse of coal fly ash, a reusable Fe-modified fly ash catalyst was synthesized for ozone catalysis degradation of chemical oxygen demand (COD) in wastewater. Through enhancement of the pretreatment procedure and FeO_x modification, the resulting fly ash with Fe modification demonstrated increased specific surface area and porosity. The presence of Fe loading significantly enhances the reactivity of surface oxidizing reactive species, particularly oxygen vacancy, leading to improved adsorption and activation properties towards ozone molecules. Sodium acetate is chosen as a probe for contaminants due to its status as a small organic substance that remains resistant to further direct oxidation by ozone. This makes it suitable for evaluating the catalyst's effectiveness in degrading chemical oxygen demand (COD). The quantitative detection of free radicals revealed the generation of $\bullet O_2^-$ was nearly 10 times that of •OH and dominated the reaction. This study showcases the potential of fly ash, an industrial byproduct, to be utilized as a cost-effective and easily prepared catalyst with consistent physical and chemical characteristics.

Keywords: coal fly ash catalyst; iron oxide; ozone catalysis; radical oxidation; COD degradation

check for updates

Citation: Chen, Y.; Chen, R.; Chang, X.; Yan, J.; Gu, Y.; Xi, S.; Sun, P.; Dong, X. Ozone Catalysis Degradation of Sodium Acetate via Vacancy-Driven Radical Oxidation over Fe-Modified Fly Ash. *Water* **2023**, *15*, 3801. https://doi.org/10.3390/w15213801

Academic Editor: Lei Qin

Received: 11 September 2023
Revised: 14 October 2023
Accepted: 16 October 2023
Published: 30 October 2023

Copyright: © 2023 by the authors. Licensee MDPI, Basel, Switzerland. This article is an open access article distributed under the terms and conditions of the Creative Commons Attribution (CC BY) license (https://creativecommons.org/licenses/by/4.0/).

1. Introduction

Fly ash is a pozzolanic mixture resulting from the combustion of coal at temperatures between 650 and 800 °C [1,2]. The significant buildup of fly ash in prominent power plants has emerged as a concern for the nearby ecosystem and public well-being. In order to reduce the problems caused by its storage, fly ash has been intensively investigated as a starting material in different fields of research. In recent years, some environmentally functional materials modified by fly ash have received increasing attention. Particular attention has been given to the development of effective adsorption materials, oxidizing catalysts, and novel advanced oxidation processes (AOP) technology using fly ash-modified materials for addressing water pollutants such as organic dyes, antibiotics, heavy metals, nitrogen, and phosphorus contaminants [3,4].

Fly ash is mainly composed of microspheres containing SiO_2 and Al_2O_3, accounting for 60~80% of the total composition [5]. While the surface of fly ash has already undergone passivation to form mullite and quartz at high temperatures, there is still potential for further exploration of its physical and chemical properties to enhance modification [6]. For instance, treating fly ash with NaOH has been found to increase its specific surface area, resulting in improved adsorption performance for cadmium in water. The maximum recorded adsorption capacities ranged from 9.18 mg/g to 48.5 mg/g [7]. Additionally, utilizing pretreated fly ash as a source of silicon and aluminum has garnered attention for catalyst synthesis, offering a means to reduce fly ash disposal by transforming it into

valuable products. For instance, fly ash was utilized as a carrier for the incorporation of $CoFe_2O_4$ to form a nanocomposite. This composite exhibited exceptional efficiency as a Fenton-like catalyst in treating wastewater from polymer-flooding processes [8]. Through meticulous optimization of reaction conditions, an impressive removal rate of 70.3% for polyacrylamide was attained. Fe_3O_4 was also deposited on fly ash and used as a catalyst for the Fenton reaction in the treatment of stabilized landfill leachate [9]. It was witnessed that fly ash-augmented Fe_3O_4 exhibited 84.7% of COD degradation at optimum pH 3, 0.05 M H_2O_2 and 1000 mg/L of catalyst and also showed 68% of total organic carbon (TOC) removal and good increment in biodegradability. In addition, different kinds of mesoporous zeolites can also be synthesized with fly ash as the silicon and aluminum source [10,11]. Some heterogeneous catalysts were prepared with the use of high-cost commercial zeolites, like SBA-15, MCM-41, or ZSM-5, as the supports and applied in a variety of wastewater treatment processes [12–14]. By using fly ash to synthesize molecular sieves and introducing some metal oxides as catalytic active centers, the cost of the water treatment reaction can be greatly reduced.

Catalytic ozone oxidation is a typical AOP that has received increasing attention in recent decades [15,16]. Different kinds of metal catalyst, including MnO_2, Fe_2O_3, Al_2O_3 and MgO, for catalytic ozonation have been reported to display both catalytic activity and superb degradation efficiency for organic pollutants in water [17–20]. However, due to their low specific surface areas and adsorption capacity, their catalytic efficiency and decontamination effectiveness were inevitably disturbed in practical application. In the course of ozone catalytic oxidation, pollutants are eliminated through the direct oxidation of ozone in water, as well as via the oxidation process triggered by reactive oxygen species (ROS) generated from ozone activation at the catalyst's active site [21]. Consequently, incorporating metal oxide as the active component in supported ozone catalysts imparts not only superior activity and stability but also cost-effectiveness.

In order to optimize the utilization of fly ash generated from power plants, this study investigates the modification of fly ash and its preparation as a catalytic material for environmental wastewater treatment. A series of catalysts loaded with iron oxide were synthesized using fly ash as the support material to investigate the process of ozone-catalyzed oxidation. To evaluate the effectiveness of the catalyst in degrading chemical oxygen demand (COD), CH_3COONa was chosen as a contaminant probe. This is because CH_3COONa is difficult to direct decomposition by ozone, and it is one of the end products of ozone oxidation of most organic pollutants [22]. The structural properties of pretreated fly ash and Fe-modified samples were characterized using techniques such as SEM, XRD, XPS, ESR, ICP, and TEM. Different reaction parameters were adjusted to evaluate their effects on ozone catalytic performance. This study showcases the potential of repurposing fly ash, an industrial waste, as a reliable and effective catalyst for ozone generation. This finding presents a novel avenue for further exploration in the field of wastewater treatment.

2. Experimental

2.1. Pretreatment of Fly Ash

The fly ash was sourced from the Zhoushan Power Plant of China's National Energy Group. Initially, it underwent immersion in a 1.2 mol/L HCl solution and agitation at a temperature of 85 °C for a duration of 2 h. Subsequently, it was rinsed with deionized water until neutralization occurred. Following drying at 50 °C, the resulting sample underwent thermal treatment at 90 °C using a hydrothermal kettle containing a 5 mol/L NaOH solution for a period of 15 h and was designated as CFA.

2.2. Synthesis of Fe-Modified Fly Ash

The CFA was impregnated with iron oxide (at mass ratios of 4%, 8%, and 12%) using a commonly reported wet impregnation method [23]. Ferric nitrate (purchased from Aladdin Biochemical Technology Co., Ltd., Shanghai, China) and CFA were accurately measured, mixed in deionized water, and continuously stirred for 5 h. The mixture was then dried at

90 °C for 10 h and calcinated at 400 °C. The resulting catalysts were labeled as Fex/CFA, where x represented the respective values of 0.04, 0.08, and 0.12.

2.3. Characterization

An X-ray powder diffractometer (XRD, Haoyuan DX-2700, Dandong, China) with Cu Ka radiation (35 kV, 25 mA) was utilized to measure the wide-angle X-Ray Diffraction patterns of various CFA samples. A scanning electron microscope (SEM, Hitachi SU-8100, Tokyo, Japan) was employed for observing and recording the morphology. Additionally, the microstructure of the Fe_x/CFA surface was further examined using a transmission electron microscope (TEM, JEM 2100, Tokyo, Japan). Nitrogen adsorption–desorption isotherms were analyzed using an ASAP 2020 analyzer (Micromeritics, Norcross, GA, USA). The specific surface area and pore size distribution were determined through the application of Brunauer–Emmett–Teller (BET) and Barrett–Joyner–Halenda (BJH) methods. A Kratos AXIS Ultra DLD spectrometer equipped with Al Ka X-rays was used for measuring X-ray photoelectron spectroscopy (XPS). Inductively Coupled Plasma Emission Spectra (ICP-OES) were obtained by employing an iCAP PRO XP ICP-OES emission spectrometer from Thermo Scientific (Waltham, MA, USA). Electron paramagnetic resonance spectroscopy measurements were conducted utilizing a A300 EPR spectrometer (Bruker, Karlsruhe, Germany).

2.4. Catalytic Ozonation Reaction

Ozone was produced from oxygen with a high level of purity at 99.9% using an ozone generator (M-1000, Tonglin, Beijing, China) in the laboratory. The ozone was introduced into a specially designed reactor through a porous titanium aerator at a concentration of 24~60 mg/L, and its concentration was determined using the sodium indigo disulphonate method. A solution of CH_3COONa (100~250 mg/L), measuring 600 mL, was added to the reactor along with a catalyst dosage ranging from 1 to 5 g/L. The pH level was adjusted by adding either NaOH or HCl solution at a concentration of 0.1 mol/L. During the catalytic ozonation process, samples were collected at specific time intervals totaling 4.0 mL each and subsequently filtered using an inorganic filter membrane that had a thickness of 0.45 μm. To immediately neutralize any remaining ozone, a solution containing $Na_2S_2O_3$ at a concentration of 0.01 mol/L was added. The elimination rate of sodium acetate was determined by employing a chemical oxygen demand (COD) tester (COD-571, Leici, Shanghai, China).

2.5. Reactive Species Detection

Nitro blue tetrazolium chloride (NBT) can react with $\bullet O_2^-$, and the formation of $\bullet O_2^-$ is detected by ultraviolet visible spectrophotometry. The specific steps are as follows: add 1.8 g of catalyst to NBT solution (4.2×10^{-5} mol/L), stir in oxygen for 60 min to achieve adsorption equilibrium, and then inject ozone. Take 4.0 mL of liquid at regular intervals and take the upper clear liquid after centrifugation. Use the ultraviolet visible spectrophotometer Sodnm (Shimadzu UV-2600, Tokyo, Japan) to record the change in its concentration at 259 nm.

Terephthalic acid (TA) can react with •OH to generate 2-hydroxyterephthalic acid (TAOH) with high fluorescence intensity. With 315 nm as the excitation wavelength, the generation of TAOH can be detected by fluorescence spectrophotometry, so that the generation of •OH in solution can be monitored. The specific operation steps were as follows: 1.8 g of catalyst was dispersed in 600 mL of solution containing 2.0 mmol/L NaOH and 2.0 mmol/L TA, the solution was stirred under oxygen for 60 min to achieve adsorption equilibrium, ozone was injected, 4.0 mL liquid was extracted at intervals, and the upper clear liquid was taken after centrifugation. A fluorescence spectrophotometer (HORIBA Fluorax-4, Tokyo, Japan) was used to measure the fluorescence intensity. Fluorescence conditions were excitation wavelength 315 nm and slit width 2 nm.

3. Results and Discussion

3.1. Enhancing the Degradation of CH_3COONa through Catalytic Ozonation

CH_3COONa is one of the end products of ozone oxidation of most organic pollutants [22], and has been used as a contaminant probe to evaluate the application prospects of fly ash-modified catalyst in ozone-catalyzed oxidative degradation of COD. Figure 1 exhibits the catalytic ozonation performance of CH_3COONa degradation over different Fe modified fly ash catalysts. A certain reduction in CH_3COONa is observed under conditions with only fly ash and ozone, which could be caused by the adsorption effect over the fly ash surface as proved by the S_{BET}, V_{total}, and pore size of pretreated fly ash being 59.64 m^2/g, 0.13 cm^3/g, and 12.76 nm, respectively (see Table 1). When only ozone and CH_3COONa were present in the reaction process, the elimination efficiency of acetic acid was inconspicuous, indicating that CH_3COONa, the end product of ozone oxidation, was resistant to further direct decomposition by ozone. After addition of different Fe-modified fly ashes as catalysts, the removal rate of CH_3COONa could be improved by a maximum of 53.3% over the $Fe_{0.08}$/CFA catalyst.

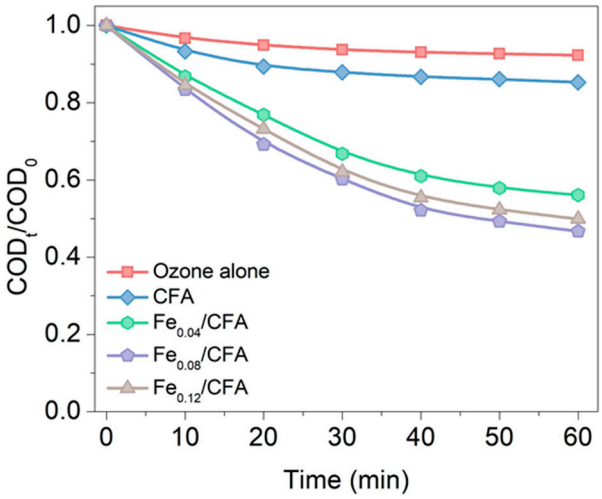


Figure 1. The degradation performance of CH_3COONa over different Fe-modified fly ash catalysts (concentration of CH_3COONa: 150 mg/L; concentration of O_3: 50 mg/L; temperature: 25 °C; pH: 7.5; catalyst dosage: 3 g/L).

Table 1. Specific surface area, porous parameters, and XPS analysis of different Fe-modified CFAs.

Samples	S_{BET} (m^2/g)	V_{total} (cm^3/g)	Pore Size (nm)	XPS Analysis				ICP Test of Fe Element (g/g)	
				Fe^{2+}/Fe^{3+}	O_{ads}	O_{sur}	O_{lat}	Theoretical	Actual
CFA	59.64	0.13	12.76	/	0.56	0.39	0.05	/	0.0098
$Fe_{0.04}$/CFA	39.14	0.11	11.46	0.85	0.45	0.42	0.13	0.04	0.034
$Fe_{0.08}$/CFA	20.26	0.08	13.44	0.88	0.33	0.52	0.15	0.08	0.061
$Fe_{0.12}$/CFA	16.37	0.06	8.47	0.83	0.40	0.39	0.21	0.12	0.087

3.2. Structure Characterization of Fe-Modified Fly Ash

The XRD patterns of pretreated fly ash and different Fe-modified fly ash catalysts are shown in Figure 2 and all display the characteristic peaks of mullite (2 theta at 16.4°, 20.8°, 25.9°, 30.7°, 33.0°, 35.2°, 40.8°, 42.4°, and 60.6°) and quartz (2 theta at 26.1° 39.2°, 53.5°, 56.8°, and 63.7°) [9]. For catalysts $Fe_{0.04}$/CFA, $Fe_{0.08}$/CFA, and $Fe_{0.12}$/CFA, 2 theta at 29.7° can be attributed to the (122) crystal plane of η-Fe_2O_3 (JCPDS No. 21-0920) [24]. Only one iron oxide diffraction peak appears, which should be due to the small loading and highly dispersed iron oxide. As observed in Figure 3's EDX-mapping, the sample of $Fe_{0.08}$/CFA reveals the uniform dispersion of Fe element consistent with that of Si, Al, and Na elements, proving that iron oxide has been successfully loaded over the surface and irregular pore structure of fly ash.

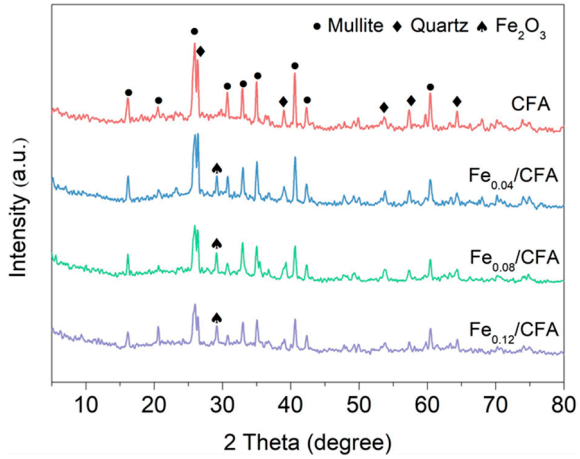


Figure 2. The XRD patterns of pretreated fly ash and different Fe-modified fly ash catalysts.

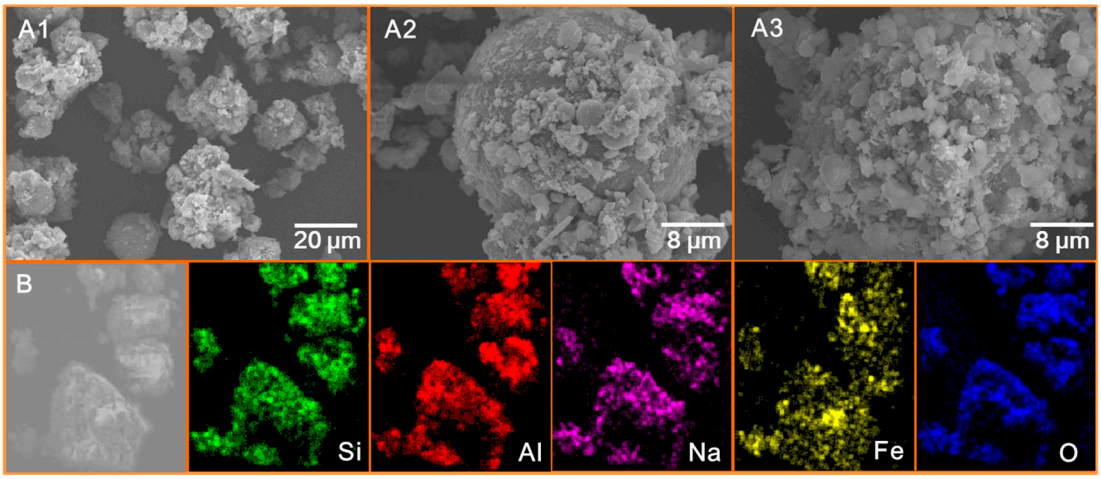


Figure 3. (**A1**–**A3**) SEM images of $Fe_{0.08}$/CFA; (**B**) EDX-mapping of $Fe_{0.08}$/CFA.

TEM was also conducted fto investigate the surface structure of the loaded iron oxide. As depicted in Figure 4, the absence of iron oxide agglomeration suggests its effective dispersion throughout the fly ash. The observed lattice spacing values of 0.324 nm and 0.272 nm were identified as corresponding to the (022) and (024) crystal planes of Fe_2O_3 [25,26], indicating the presence of amorphous iron oxide formation. All of the iron-loaded fly ash samples were also tested for their actual iron content by ICP. As listed in Table 1, there is little difference between the actual iron content and the theoretical iron content, which means the above synthetic method is feasible. In addition, the fly ash itself (CFA) also has a number of impurities, which derive from metal impurities, including Ca, Mg, Fe, etc. The contents of these impurities were greatly weakened by pretreatment of fly ash by acidification and alkalinization.

XPS analyses were also conducted to investigate the surface element state over different Fe-modified samples. As shown in Figure 5A, all of the Fe-modified samples exhibit a peak at a binding energy of ca.720 eV ascribed to Fe 2p compared with the CFA sample [24], indicating the existence of surface iron oxide. In Figure 5B,C, the Fe 2p and O 1s spectra were subjected to deconvolution using a Gaussian peaks fitting technique following Shirley background subtraction. For spectra of Fe 2p, the peaks of Fe 2p3/2 and Fe 2p1/2 were located at 711 eV and 725 eV, respectively, and the binding energy peaks at 711.1 eV and 713.0 were attributed to Fe(II) and Fe(III) species [24–26]. The O 1s spectra can be divided into three peaks at ranges of 529.8~530.3 eV, 530.8~531.3 eV, and 532.0~532.5 eV, ascribed to lattice oxygen (O_{lat}) [27], surface chemisorbed oxygen (O_{sur})-like OH^-, O_2^-,

CO_3^{2-}, oxygen vacancy (O_V) [28], and the surface-adsorbed oxygen-like adsorbed water species [29], respectively.

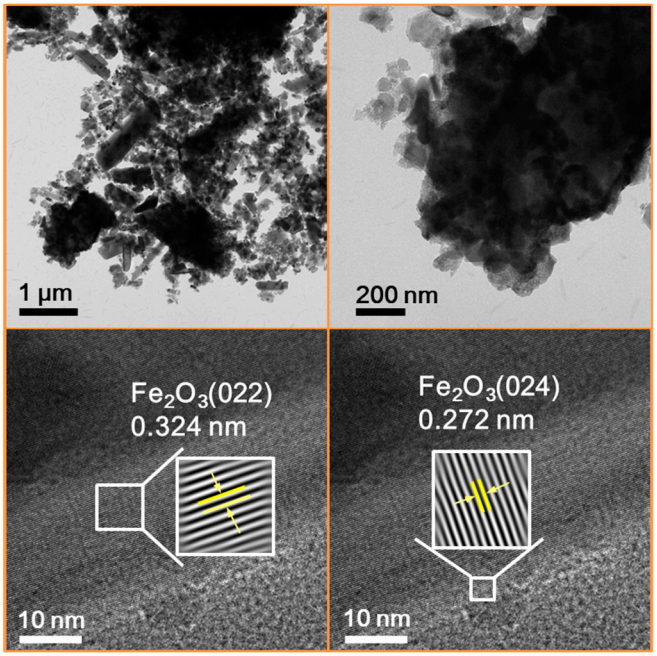


Figure 4. HR-TEM images of $Fe_{0.08}$/CFA.

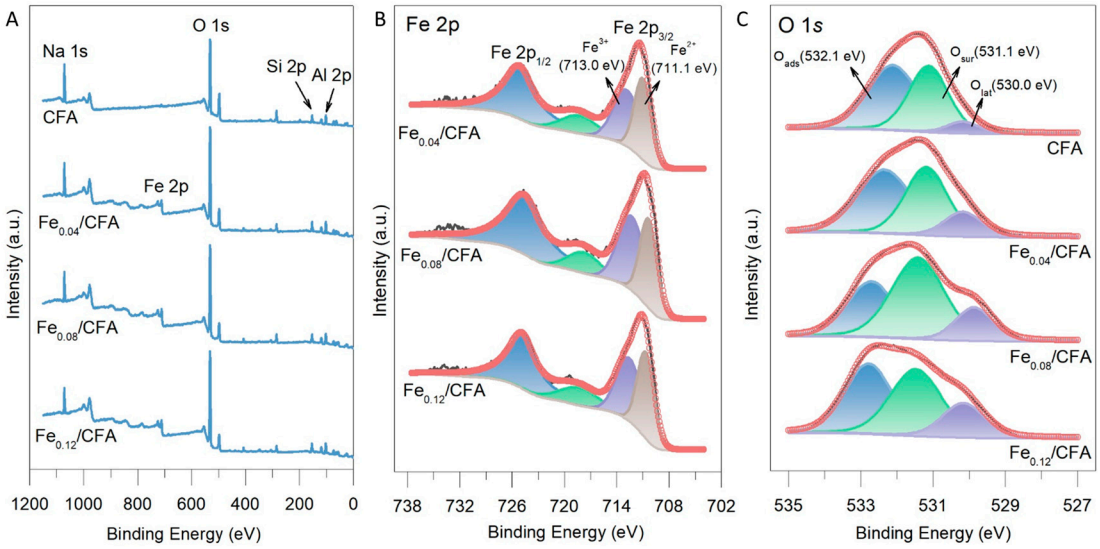


Figure 5. XPS spectra of CFA and different Fe- modified CFAs: (**A**) survey; (**B**) Fe 2p; and (**C**) O 1s.

It can be judged from Table 1, that the change in Fe^{2+}/Fe^{3+} and O_{sur} is consistent with the increase in Fe content. When the Fe content increased from 4 wt% to 8 wt%, the ratio of Fe^{2+}/Fe^{3+} also increased from 0.85 to 0.88. As reported in a previous study [30], Fe^{2+} could provide electrons for the decomposition of O_3 and be transformed into Fe^{3+}. A higher redox reaction of Fe^{2+}/Fe^{3+} could maintain the electrostatic equilibrium of the catalyst surface and improve the performance of ozone catalytic oxidation [31,32]. At this time, we can also find that the $Fe_{0.08}$/CFA sample has the maximum amount of O_{sur}. During the ozone catalysis process, the oxygen vacancy derived from O_{sur} plays an important role in converting the absorbed O_3 into $\bullet O_2^-$ and •OH [28], which then further decompose the organic content of water. The ESR spectra in Figure 6 confirm that the $Fe_{0.08}$/CFA sample exhibits the strongest oxygen vacancy strength among all of the Fe-modified catalysts, with a pair of steep peaks

in accordance with g = 2.002, an indication of electron trapping at oxygen vacancies [33]. Thus, the better CH_3COONa degradation performance of $Fe_{0.08}$/CFA exhibited in Figure 1 could be mainly due to the above two reasons.

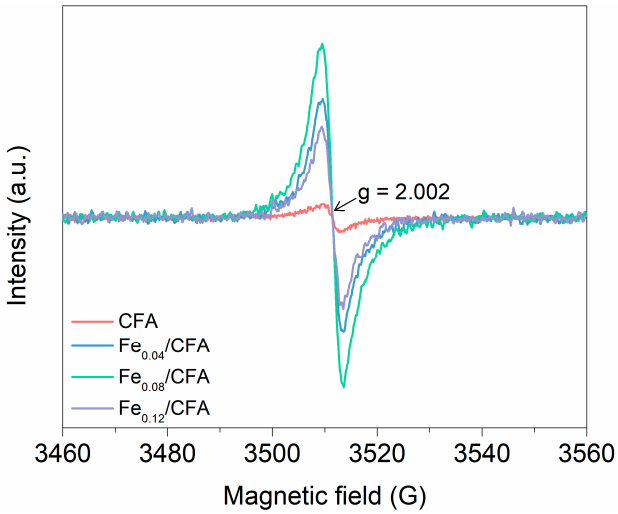


Figure 6. ESR spectra of CFA and different Fe-modified CFAs.

For the $Fe_{0.12}$/CFA sample, the change in Fe^{2+}/Fe^{3+} and O_{sur} began to decrease with a further increase in Fe content. However, there was a certain degree of improvement in O_{lat}. This could be caused by excessive Fe loading, leading to particle clustering and decreased dispersion over the surface of fly ash, which thus caused more bulk phase lattice oxygen to be produced at the surface due to metal clusters. The significantly decreased S_{BET} and pore size of $Fe_{0.12}$/CFA compared with that of $Fe_{0.04}$/CFA and $Fe_{0.08}$/CFA also implies that a large number of iron oxide clusters may accumulate in the surface channel of CFA.

3.3. Effect of Reaction Parameters on the Degradation Efficiency of CH_3COONa

The $Fe_{0.08}$/CFA was selected as the best catalyst for ozone-catalyzed oxidation of CH_3COONa to investigate the effects of different reaction parameters on performance. As shown in Figure 7A, the CH_3COONa removal efficiencies obtained after 60 min at ozone dosages of 24, 37, 50, and 60 mg/L were equal to 45.2%, 49.8%, 53.3%, and 53.1%, respectively. It can be found that the CH_3COONa-removal efficiency of $Fe_{0.08}$/CFA increases with an increase in the ozone dosage from 24 to 50 mg/L and then stabilizes at an ozone dosage of 60 mg/L. The degradation of CH_3COONa required ozone adsorption onto the catalyst surface and further activation to form effective free radicals to decompose CH_3COONa [34]. When the ozone concentration was increased to 60 mg/L, the ozone adsorption and deionization over the surface of $Fe_{0.08}$/CFA could be considered to reach dynamic equilibrium, and the oxidation-active species formed from ozone for the oxidation of CH_3COONa would not increase further. Therefore, the ozone concentration of 50 mg/L was selected to further investigate the influence of $Fe_{0.08}$/CFA dosage. Figure 7B reveals that the catalyst $Fe_{0.08}$/CFA, at a concentration of 3.0 g/L, has a CH_3COONa-removal efficiency of 53.3% in 60 min, much higher than $Fe_{0.08}$/CFA at a concentration of 1.0 g/L. When the ozone-oxidizing agent was sufficient, increasing the catalyst dosage could increase the number of catalytic active sites, resulting in the generation of more oxidation-active species and improved CH_3COONa-removal efficiency. However, when the $Fe_{0.08}$/CFA dosage exceeded the optimal value, the extra active sites to be reacted are invalid. Thus, $Fe_{0.08}$/CFA at a dosage of 5.0 g/L did not result in better CH_3COONa-removal efficiency.

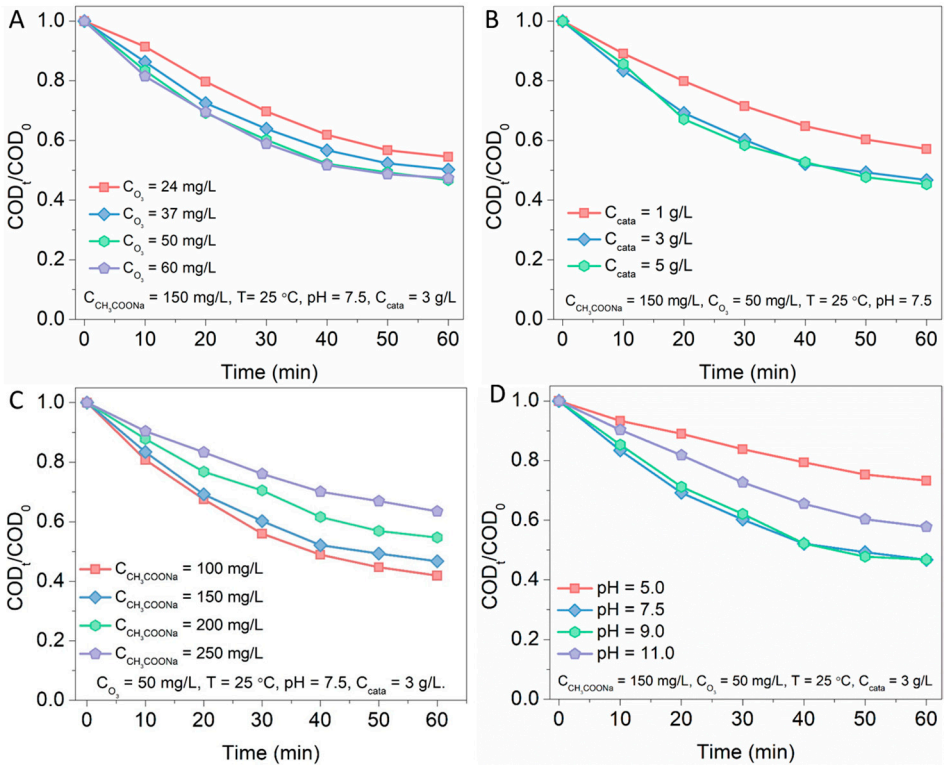


Figure 7. (**A**) Effect of initial ozone concentration on removal efficiency of CH_3COONa. (**B**) Effect of initial catalyst dosage on removal efficiency of CH_3COONa. (**C**) Effect of initial CH_3COONa concentration on performance of $Fe_{0.08}$/CFA. (**D**) Effect of pH value on removal efficiency of CH_3COON.

The influence of different initial CH_3COONa concentrations on the performance of $Fe_{0.08}$/CFA was also studied. As shown in Figure 7C, the removal efficiencies of CH_3COONa achieved after 60 min at initial concentrations of 100, 150, 200, and 250 mg/L are equal to 58.1%, 53.3%, 45.3%, and 36.5%, respectively. The higher removal rates observed at lower CH_3COONa concentrations are due to higher ratios of oxidation-active species (like $\bullet O_2^-$ or •OH) to CH_3COONa molecules (that is, the probability of collision of each CH_3COONa molecule with $\bullet O_2^-$ or •OH species is increased with decreasing CH_3COONa content) [24]. On the other hand, the increased CH_3COONa concentration will also result in competitive adsorption with the dissolved ozone, which thus limits the generation of oxidation-active species and restricts the degradation of CH_3COONa [35].

The solution's pH is regarded as a crucial element that impacts the ozone catalytic process, exerting a significant influence on the routes of ozone reaction. As shown in Figure 7D, the performance of $Fe_{0.08}$/CFA is obviously suppressed in acidic and alkaline circumstances. The removal efficiency of CH_3COONa decreased to 26.7% and 42.2% with pH values at 5.0 and 11.0, respectively. In an acidic environment, ozone molecules have a tendency to react selectively with organic matter containing specific functional groups, such as electrophilic groups, nucleophilic groups, and to take part in dipolar addition reactions in acid solution [36]. This will affect the adsorption efficiency of ozone on the catalyst surface and its further dissociation to form active free radicals such as $\bullet O_2^-$ or •OH [37]. On the contrary, the suppressed performance of $Fe_{0.08}$/CFA at pH = 11.0 also suggests that the excess hydroxide in solution will cause insoluble iron hydroxide formation from the loaded Fe ions [9,24], which covers the catalyst surface and reduces the number of active sites. When the pH value was 7 or 9, that the degradation efficiency of CH_3COONa was not significantly affected, indicating that the synthesized $Fe_{0.08}$/CFA has good applicability over a wide pH range on either side of the neutral condition.

3.4. Reaction Mechanism Study

The main active species for oxidation of CH_3COONa over $Fe_{0.08}$/CFA was revealed by adding different scavengers. As shown in Figure S1, p-benzoquinone (p-BQ), tert-butyl alcohol (TBA), and L-histidine (L-HIS) were used to quench $\bullet O_2^-$, •OH, and singlet oxygen ($^1O_2$), respectively [25]. After quenching $^1O_2$, the removal efficiency of CH_3COONa was slightly decreased; however, it was greatly suppressed without $\bullet O_2^-$ and •OH. This result suggests the main active species for CH_3COONa degradation over $Fe_{0.08}$/CFA were $\bullet O_2^-$ and •OH. The generation of reactive oxygen species was also characterized by EPR technology, where 5,5-dimethyl-1-pyrroline N-oxide (DMPO) can trap $\bullet O_2^-$ and •OH to form adducts that have 1:1:1:1 and 1:2:2:1 EPR signals [38]. Figure 8(A1,B1) shows that the corresponding peaks can be only produced with the existence of $Fe_{0.08}$/CFA, suggesting that ozone was stimulated to form related free radicals after adsorption over the catalyst surface.

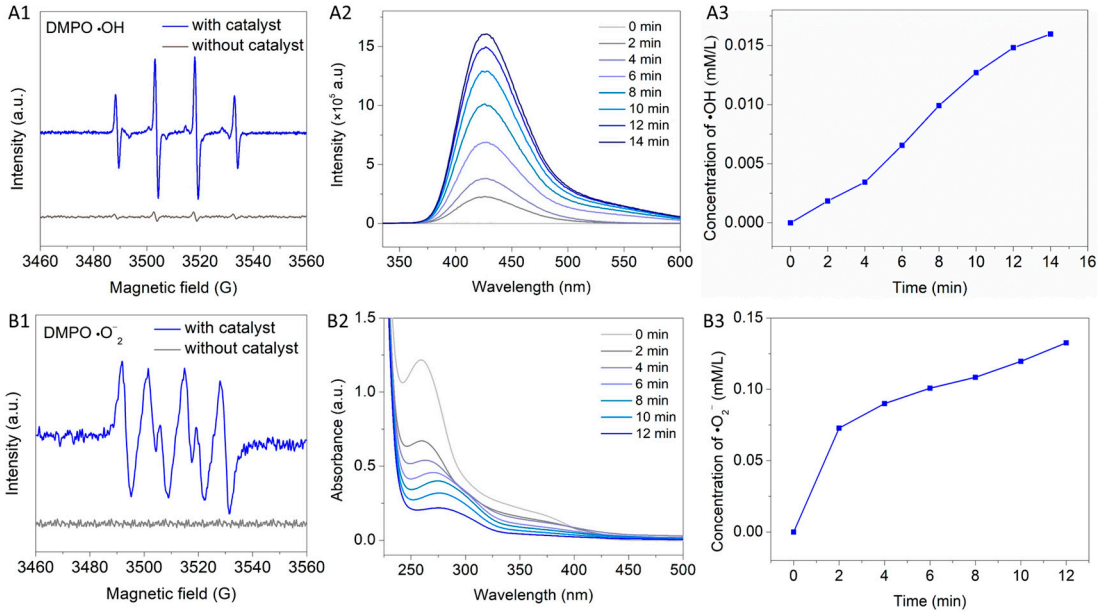


Figure 8. EPR spectra of DMPO−•OH (**A1**) and DMPO-$\bullet O_2^-$ (**B1**). Absorption spectra of NBT solution (**A2**) and PL spectra of TA solution (**B2**) with $Fe_{0.08}$/CFA. The quantitative concentration of •OH (**A3**) and $\bullet O_2^-$ (**B3**) via PL spectra of TA and absorption spectra of NBT at different times.

The produced $\bullet O_2^-$ and •OH over catalyst $Fe_{0.08}$/CFA were also quantified by chemical titration. As shown in Figure 8(A2), TA could be oxidized to 2-hydroxyterephthalic acid (TAOH), which had a characteristic photoluminescence (PL) signal centered at 425 nm [39]. With the extension of reaction time, the amount of •OH was also gradually increased, and the final •OH concentration could be achieved at 0.015 mmol/L within 14 min (see Figure 8(A3)). We also demonstrated $\bullet O_2^-$ production by the NBT method. After the NBT had reacted with $\bullet O_2^-$, and the absorbance of NBT at 259 nm (Figure 8(B2)) gradually decreased with the extension of reaction time, suggesting the steady generation of $\bullet O_2^-$ in solution [40]. The maximum amount of generated $\bullet O_2^-$ could be achieved at 0.16 mmol/L within 12 min (see Figure 8(B3)). Obviously, the production concentration of $\bullet O_2^-$ is nearly 10 times that of •OH, which indicates that $\bullet O_2^-$ plays a more dominant role in the oxidation of CH_3COONa. This result is also consistent with the experimental results exhibited in Figure S1: after quenching of $\bullet O_2^-$ by p-BQ, the degradation efficiency of CH_3COONa would be seriously affected.

4. Conclusions

We developed a supported ozone catalyst by utilizing fly ash as a carrier and incorporating iron oxide as the active phase. The structural characteristics of pretreated fly ash

and Fe-modified samples were assessed using various techniques such as SEM, XRD, TEM, ICP, XPS, ESR, etc. The S_{BET} of fly ash samples could reach 59.6 m^2/g, which provided better surface circumstances for loading of iron oxide. CH_3COONa was selected as a targeted pollutant for assessing the ozone catalysis performance of Fe-modified samples, and the best removal rate of CH_3COONa was obtained at 53.3% over $Fe_{0.08}$/CFA catalyst. A higher ratio of Fe^{2+}/Fe^{3+} over $Fe_{0.08}$/CFA improved the formation of $O_{(V)}$, which had an impact on converting the absorbed O_3 into $\bullet O_2^-$ and •OH. The effect of pH on reaction performance was also verified. Under neutral conditions, $Fe_{0.08}$/CFA could obtain the best performance for removal of CH_3COONa, excluding the formation of ferric hydroxide under alkaline conditions and the inhibition of ozone adsorption under acidic conditions. The generation of $\bullet O_2^-$ and •OH over oxygen vacancy with the existence of ozone were further investigated in detail, revealing that the generation of $\bullet O_2^-$ was nearly 10 times that of •OH and dominated the reaction. According to current reports [32], this large amount of produced $\bullet O_2^-$ could be due to the mechanism of $O_{(V)} + H_2O \rightarrow Surface–OH_2^+$, $Surface–OH_2^+ + O_3 \rightarrow Surface–\bullet O_2^- + \bullet OH_3$ and $\bullet OH_3 \rightarrow O_2 + \bullet OH$. In summary, this work confirms effective COD degradation by modified fly ash, which expands the vision of increasing the added value of fly ash and the new technology for the wastewater treatment of CH_3COONa could be seriously affected.

Supplementary Materials: The following supporting information can be downloaded at: https://www.mdpi.com/article/10.3390/w15213801/s1, Figure S1: Removal rate of CH_3COONa over $Fe_{0.08}$/CFA under the condition of scavengers added (concentration of CH_3COONa: 150 mg/L, concentration of O_3: 50 mg/L, temperature: 25 °C, pH: 7.5, catalyst dosage: 3 g/L).

Author Contributions: Conceptualization, Y.C. and R.C.; methodology, Y.C. and R.C.; validation, X.C., J.Y. and X.D.; investigation, Y.C. and X.D.; writing—original draft preparation, Y.C.; writing—review and editing, R.C. and P.S.; supervision, Y.G., P.S. and S.X.; funding acquisition, Y.C., X.D. and P.S. All authors have read and agreed to the published version of the manuscript.

Funding: This research received financial support from the R&D Program of Zhejiang Tiandi Environmental Protection Technology Co., Ltd., China (Project Code: ZNKJ-2022-06; TD-KJ-22-006) and was also funded through preferential grants for Postdoctoral Research Projects in Zhejiang Province, China (Grant Number: ZJ2021052).

Data Availability Statement: Data is available through the author.

Conflicts of Interest: The authors declare no conflict of interest.

References

1. You, S.; Ho, S.W.; Li, T.; Maneerung, T.; Wang, C.-H. Techno-economic analysis of geopolymer production from the coal fly ash with high iron oxide and calcium oxide contents. *J. Hazard. Mater.* **2019**, *361*, 237–244. [CrossRef]
2. Forminte, L.; Ciobanu, G.; Buema, G.; Lupu, N.; Chiriac, H.; de Castro, C.G.; Harja, M. New materials synthesized by sulfuric acid attack over power plant fly ash. *Rev. Chim.* **2020**, *71*, 48–58. [CrossRef]
3. Cheng, Y.; Wang, B.; Yan, P.; Shen, J.; Kang, J.; Zhao, S.; Zhu, X.; Shen, L.; Wang, S.; Shen, Y. In-situ formation of surface reactive oxygen species on defective sites over N-doped biochar in catalytic ozonation. *Chem. Eng. J.* **2023**, *454*, 140232. [CrossRef]
4. Yao, Z.T.; Ji, X.; Sarker, P.; Tang, J.; Ge, L.; Xia, M.; Xi, Y. A comprehensive review on the applications of coal fly ash. *Earth-Sci. Rev.* **2015**, *141*, 105–121. [CrossRef]
5. Feng, W.; Wan, Z.; Daniels, J.; Li, Z.; Xiao, G.; Yu, J.; Xu, D.; Guo, H.; Zhang, D.; May, E.F. Synthesis of high quality zeolites from coal fly ash: Mobility of hazardous elements and environmental applications. *J. Clean. Prod.* **2018**, *202*, 390–400. [CrossRef]
6. Wang, L.; Huang, X.; Zhang, J.; Wu, F.; Liu, F.; Zhao, H.; Hu, X.; Zhao, X.; Li, J.; Ju, X. Stabilization of lead in waste water and farmland soil using modified coal fly ash. *J. Clean. Prod.* **2021**, *314*, 127957. [CrossRef]
7. Buema, G.; Lupu, N.; Chiriac, H.; Ciobanu, G.; Bucur, R.-D.; Bucur, D.; Favier, L.; Harja, M. Performance assessment of five adsorbents based on fly ash for removal of cadmium ions. *J. Mol. Liq.* **2021**, *333*, 115932. [CrossRef]
8. Wang, N.; Sun, X.; Zhao, Q.; Wang, P. Treatment of polymer-flooding wastewater by a modified coal fly ash-catalysed Fenton-like process with microwave pre-enhancement: System parameters, kinetics, and proposed mechanism. *Chem. Eng. J.* **2021**, *406*, 126734. [CrossRef]
9. Niveditha, S.; Gandhimathi, R. Flyash augmented Fe_3O_4 as a heterogeneous catalyst for degradation of stabilized landfill leachate in Fenton process. *Chemosphere* **2020**, *242*, 125189. [CrossRef]

10. Gupta, P.K.; Mahato, A.; Oraon, P.; Gupta, G.K.; Maity, S. Coal fly ash-derived mesoporous SBA-15 as support material for production of liquid hydrocarbon through Fischer–Tropsch route. *Asia-Pac. J. Chem. Eng.* **2020**, *15*, e2471. [CrossRef]
11. Sikarwar, P.; Kumar, U.A.; Gosu, V.; Subbaramaiah, V. Catalytic oxidative desulfurization of DBT using green catalyst (Mo/MCM-41) derived from coal fly ash. *J. Environ. Chem. Eng.* **2018**, *6*, 1736–1744. [CrossRef]
12. Yuan, S.; Wang, M.; Liu, J.; Guo, B. Recent advances of SBA-15-based composites as the heterogeneous catalysts in water decontamination: A mini-review. *J. Environ. Manag.* **2020**, *254*, 109787. [CrossRef]
13. Sun, X.; Xu, D.; Dai, P.; Liu, X.; Tan, F.; Guo, Q. Efficient degradation of methyl orange in water via both radical and non-radical pathways using Fe-Co bimetal-doped MCM-41 as peroxymonosulfate activator. *Chem. Eng. J.* **2020**, *402*, 125881. [CrossRef]
14. Mohammadi, R.; Feyzi, M.; Joshaghani, M. Synthesis of ZnO-magnetic/ZSM-5 and its application for removal of disperse Blue 56 from contaminated water. *Chem. Eng. Process.* **2020**, *153*, 107969. [CrossRef]
15. Yuan, L.; Shen, J.; Yan, P.; Chen, Z. Interface mechanisms of catalytic ozonation with amorphous iron silicate for removal of 4-chloronitrobenzene in aqueous solution. *Environ. Sci. Technol.* **2018**, *52*, 1429–1434. [CrossRef] [PubMed]
16. Zhang, T.; Li, C.; Ma, J.; Tian, H.; Qiang, Z. Surface hydroxyl groups of synthetic α-FeOOH in promoting OH generation from aqueous ozone: Property and activity relationship. *Appl. Catal. B Environ.* **2008**, *82*, 131–137. [CrossRef]
17. Zhu, H.; Ma, W.; Han, H.; Han, Y.; Ma, W. Catalytic ozonation of quinoline using nano-MgO: Efficacy, pathways, mechanisms and its application to real biologically pretreated coal gasification wastewater. *Chem. Eng. J.* **2017**, *327*, 91–99. [CrossRef]
18. Nawaz, F.; Cao, H.; Xie, Y.; Xiao, J.; Chen, Y.; Ghazi, Z.A. Selection of active phase of MnO_2 for catalytic ozonation of 4-nitrophenol. *Chemosphere* **2017**, *168*, 1457–1466. [CrossRef]
19. Kermani, M.; Kakavandi, B.; Farzadkia, M.; Esrafili, A.; Jokandan, S.F.; Shahsavani, A. Catalytic ozonation of high concentrations of catechol over TiO_2@Fe_3O_4 magnetic core-shell nanocatalyst: Optimization, toxicity and degradation pathway studies. *J. Clean. Prod.* **2018**, *192*, 597–607. [CrossRef]
20. Ncanana, Z.; Pullabhotla, V.R. Oxidative degradation of m-cresol using ozone in the presence of pure γ-Al_2O_3, SiO_2 and V_2O_5 catalysts. *J. Environ. Chem. Eng.* **2019**, *7*, 103072. [CrossRef]
21. Kruanak, K.; Jarusutthirak, C. Degradation of 2, 4, 6-trichlorophenol in synthetic wastewater by catalytic ozonation using alumina supported nickel oxides. *J. Environ. Chem. Eng.* **2019**, *7*, 102825. [CrossRef]
22. Shen, T.; Su, W.; Yang, Q.; Ni, J.; Tong, S. Synergetic mechanism for basic and acid sites of MgM_xO_y (M = Fe, Mn) double oxides in catalytic ozonation of p-hydroxybenzoic acid and acetic acid. *Appl. Catal. B Environ.* **2020**, *279*, 119346. [CrossRef]
23. Sun, P.; Zhai, S.; Chen, J.; Yuan, J.; Wu, Z.; Weng, X. Development of a multi-active center catalyst in mediating the catalytic destruction of chloroaromatic pollutants: A combined experimental and theoretical study. *Appl. Catal. B Environ.* **2020**, *272*, 119015. [CrossRef]
24. Wang, N.; Jin, L.; Li, C.; Liang, Y.; Wang, P. Preparation of coal fly ash-based Fenton-like catalyst and its application for the treatment of organic wastewater under microwave assistance. *J. Clean. Prod.* **2022**, *342*, 130926. [CrossRef]
25. Li, M.; Yang, K.; Huang, X.; Liu, S.; Jia, Y.; Gu, P.; Miao, H. Efficient degradation of trimethoprim by catalytic ozonation coupled with Mn/FeOx-functionalized ceramic membrane: Synergic catalytic effect and enhanced anti-fouling performance. *J. Colloid Interf. Sci.* **2022**, *616*, 440–452. [CrossRef] [PubMed]
26. Li, K.; Feng, D.; Tong, Y. Hierarchical metal sulfides heterostructure as superior bifunctional electrode for overall water splitting. *ChemSusChem* **2022**, *15*, e202200590. [CrossRef] [PubMed]
27. Cheng, F.; Zhang, T.; Zhang, Y.; Du, J.; Han, X.; Chen, J. Enhancing electrocatalytic oxygen reduction on MnO_2 with vacancies. *Angew. Chem. Int. Ed.* **2013**, *125*, 2534–2537. [CrossRef]
28. Liang, L.; Cao, P.; Qin, X.; Wu, S.; Bai, H.; Chen, S.; Yu, H.; Su, Y.; Quan, X. Oxygen vacancies-driven nonradical oxidation pathway of catalytic ozonation for efficient water decontamination. *Appl. Catal. B Environ.* **2023**, *325*, 122321. [CrossRef]
29. Yu, J.; Li, X.; Wu, M.; Lin, K.; Xu, L.; Zeng, T.; Shi, H.; Zhang, M. Synergistic role of inherent calcium and iron minerals in paper mill sludge biochar for phosphate adsorption. *Sci. Total. Environ.* **2022**, *834*, 155193. [CrossRef]
30. Cai, C.; Duan, X.; Xie, X.; Kang, S.; Liao, C.; Dong, J.; Liu, Y.; Xiang, S.; Dionysiou, D.D. Efficient degradation of clofibric acid by heterogeneous catalytic ozonation using $CoFe_2O_4$ catalyst in water. *J. Haz. Mat.* **2021**, *410*, 124604. [CrossRef]
31. Li, Z.; Lyu, J.; Ge, M. Synthesis of magnetic Cu/$CuFe_2O_4$ nanocomposite as a highly efficient Fenton-like catalyst for methylene blue degradation. *J. Mater. Sci.* **2018**, *53*, 15081–15095. [CrossRef]
32. Zhang, L.; Li, Y.; Guo, J.; Kan, Z.; Jia, Y. Catalytic ozonation mechanisms of Norfloxacin using Cu–$CuFe_2O_4$. *Environ. Res.* **2023**, *216*, 114521. [CrossRef]
33. Gao, P.; Zhang, Z.; Feng, L.; Liu, Y.; Du, Z.; Zhang, L. Novel Ti_3C_2/Bi@BiOI nanosheets with gradient oxygen vacancies for the enhancement of spatial charge separation and photocatalytic performance: The roles of reactive oxygen and iodine species. *Chem. Eng. J.* **2021**, *426*, 130764. [CrossRef]
34. Liu, J.; Ke, L.; Liu, J.; Sun, L.; Yuan, X.; Li, Y.; Xia, D. Enhanced catalytic ozonation towards oxalic acid degradation over novel copper doped manganese oxide octahedral molecular sieves nanorods. *J. Haz. Mater.* **2019**, *371*, 42–52. [CrossRef]
35. Saputra, E.; Muhammad, S.; Sun, H.; Ang, H.-M.; Tadé, M.O.; Wang, S. Manganese oxides at different oxidation states for heterogeneous activation of peroxymonosulfate for phenol degradation in aqueous solutions. *Appl. Catal. B Environ.* **2013**, *142*, 729–735. [CrossRef]
36. Wang, Y.; Yang, W.; Yin, X.; Liu, Y. The role of Mn-doping for catalytic ozonation of phenol using Mn/γ-Al_2O_3 nanocatalyst: Performance and mechanism. *J. Environ. Chem. Eng.* **2016**, *4*, 3415–3425. [CrossRef]

37. Ma, N.; Ru, Y.; Weng, M.; Chen, L.; Chen, W.; Dai, Q. Synergistic mechanism of supported Mn–Ce oxide in catalytic ozonation of nitrofurazone wastewater. *Chemosphere* **2022**, *308*, 136192. [CrossRef]
38. Liu, Y.; Bian, C.; Li, Y.; Sun, P.; Xiao, Y.; Xiao, X.; Wang, W.; Dong, X. Aminobenzaldehyde convelently modified graphitic carbon nitride photocatalyst through Schiff base reaction: Regulating electronic structure and improving visible-light-driven photocatalytic activity for moxifloxacin degradation. *J. Colloid. Interface Sci.* **2023**, *630*, 867–878. [CrossRef]
39. Li, Y.; Sun, P.; Liu, T.; Cheng, L.; Chen, R.; Bi, X.; Dong, X. Efficient photothermal conversion for oxidation removal of formaldehyde using an rGO-CeO_2 modified nickel foam monolithic catalyst. *Sep. Purif. Technol.* **2023**, *311*, 123236. [CrossRef]
40. Bian, C.; Zhou, B.; Mo, F.; Liu, X.; Sun, P.; Dong, X. Post-synthetically covalent modification of g-C_3N_4 to regulate electronic structure and investigation of photocatalytic activity for eliminating antibiotics. *Sep. Purif. Technol.* **2023**, *325*, 124556. [CrossRef]

Disclaimer/Publisher's Note: The statements, opinions and data contained in all publications are solely those of the individual author(s) and contributor(s) and not of MDPI and/or the editor(s). MDPI and/or the editor(s) disclaim responsibility for any injury to people or property resulting from any ideas, methods, instructions or products referred to in the content.